A Deep Search for Five Molecules in the 49 Ceti Debris Disk

Jessica Klusmeyer,[1,2] A. Meredith Hughes,[1] Luca Matrà,[3,4]
Kevin Flaherty,[5] Ágnes Kóspál,[6,7,8] Attila Moór,[6,8] Aki Roberge,[9]
Karin Öberg,[3] Aaron Boley,[10] Jacob White,[11,12] David Wilner,[3] and
Péter Ábrahám[6,8]

[1]*Department of Astronomy, Van Vleck Observatory, Wesleyan University, 96 Foss Hill Drive, Middletown, CT 06459, USA*

[2]*NSF's NOIRLab, 950 N. Cherry Ave., Tucson, AZ 85719, USA*

[3]*Center for Astrophysics | Harvard & Smithsonian, 60 Garden Street, Cambridge, MA 02138, USA*

[4]*Centre for Astronomy, School of Physics, National University of Ireland Galway, University Road, Galway, Ireland*

[5]*Department of Astronomy and Department of Physics, Williams College, Williamstown, MA 01267, USA*

[6]*Konkoly Observatory, Research Centre for Astronomy and Earth Sciences, Eötvös Loránd Research Network (ELKH), Konkoly-Thege Miklós út 15-17, H-1121 Budapest, Hungary*

[7]*Max Planck Institute for Astronomy, Königstuhl 17, D-69117 Heidelberg, Germany*

[8]*ELTE Eötvös Loránd University, Institute of Physics, Pázmány Péter sétány 1/A, 1117 Budapest, Hungary*

[9]*Exoplanets & Stellar Astrophysics Laboratory, NASA Goddard Space Flight Center, Code 667, Greenbelt, MD 20771, USA*

[10]*Department of Physics and Astronomy, University of British Columbia, Vancouver BC, Canada*

[11]*National Radio Astronomy Observatory, 520 Edgemont Rd., Charlottesville, VA, 22903, USA*

[12]*Jansky Fellow of the National Radio Astronomy Observatory*

ABSTRACT

Surprisingly strong CO emission has been observed from more than a dozen debris disks around nearby main-sequence stars. The origin of this CO is unclear, in particular whether it is left over from the protoplanetary disk phase or is second-generation material released from collisions between icy bodies like debris dust. The primary unexplored avenue for distinguishing the origin of the material is understanding its molecular composition. Here we present a deep search for five molecules (CN, HCN, HCO^+, SiO, and CH_3OH) in the debris disk around 49 Ceti. We take advantage of the high sensitivity of the Atacama Large Millimeter/submillimeter Array (ALMA) at Band 7 to integrate for 3.2 hours at modest spatial (1") and spectral ($0.8\,\mathrm{km\,s^{-1}}$) resolution. Our search yields stringent upper limits on the flux of all surveyed molec-

ular lines, which imply abundances relative to CO that are orders of magnitude lower than those observed in protoplanetary disks and Solar System comets, and also those predicted in outgassing models of second-generation material. However, if CI shielding is responsible for extending the lifetime of any CO produced in second-generation collisions, as proposed by Kral et al. (2019), then the line ratios do not reflect true ice phase chemical abundances, but rather imply that CO is shielded by its own photodissociation product, CI, but other molecules are rapidly photodissociated by the stellar and interstellar radiation field.

1. INTRODUCTION

The dusty debris disks around main sequence stars are hallmarks of mature planetary systems. The small quantity ($<< 1\,\mathrm{M}_\oplus$) of dust in debris disks is generated by destructive processes involving grinding collisions of planetesimals (Hughes et al. 2018, and references therein). Recent observations have revealed that the dust is commonly accompanied by detectable amounts of molecular gas (e.g., Zuckerman et al. 1995; Moór et al. 2011, 2017). The only molecular species so far detected is CO, which is detected most commonly around A- and B-type stars (Lieman-Sifry et al. 2016) despite their harsh UV radiation fields that ought to photodissociate the gas on timescales much shorter than the age of the star (e.g., Visser et al. 2009; Kóspál et al. 2013). Surprisingly, some of these systems exhibit CO emission comparable to that from the protoplanetary disks around pre-main sequence stars.

Work to understand the origin and implications of the molecular gas in debris disks has centered around the question of whether the gas is effectively primordial, i.e., surviving from the protoplanetary disk phase and therefore H_2-dominated, or secondary, i.e., produced in destructive processes like the dust in debris disks and therefore H_2-poor. The former category is sometimes referred to as "hybrid" disks (e.g., Kóspál et al. 2013), since it would imply the coexistence of primordial gas and secondary dust.

Observationally, it is difficult to distinguish the origin of the gas on the basis of CO observations alone, although the weight of the evidence leans towards it being second-generation origin. The low excitation temperatures are suggestive of a low H_2 gas mass, unlike the LTE conditions in protoplanetary disks (Kóspál et al. 2013). A secondary origin is also supported by the unresolved scale height in the 49 Ceti disk at a resolution of 0.″4 that suggests a high mean molecular weight (Hughes et al.

2017). The presence of large amounts of CI gas in at least two systems has also been interpreted as evidence of second-generation origin (Higuchi et al. 2017a). Certainly the asymmetries associated with individual systems like β Pic and Fomalhaut are consistent with a second-generation origin (Dent et al. 2014; Matrà et al. 2017a). On the other hand, the gas release rates required to sustain the large mass CO for the brightest systems, which can require vaporizing a small comet every few seconds if the CO is unshielded or a Hale-Bopp-size comet roughly once an hour (Zuckerman & Song 2012; Kóspál et al. 2013), are difficult to reconcile with the putative mass reservoirs in debris disks and the high frequency with which gas is observed.

Even if the origin of the gas is secondary, multiple mechanisms have been proposed to generate secondary gas. These mechanisms include photodesorption (Grigorieva et al. 2007), collisional vaporization of icy dust grains (Czechowski & Mann 2007), and low-velocity collisions, either at the site of a resonant point with an unseen planet (Dent et al. 2014) or as the result of a major collision between planetary embryos (Jackson et al. 2014), collisional desorption from comets (Zuckerman & Song 2012), or sublimation of comets in the inner regions of the system to explain absorption features (Beust et al. 1990). Notably, Kral et al. (2017) developed a model based on the destruction of volatile-rich planetesimals that can explain the CO, C, and O content of most of the debris disks observed to date. In that work they suggest that some of the higher-mass sources may be hybrid disks. However, an extension of this basic model posits that even young debris disks with protoplanetary-level CO masses may in fact be composed of second-generation gas shielded by CI (Kral et al. 2019).

The chemical composition of the molecular gas is a relatively unexplored dimension of the properties of gas-bearing debris disks that can provide insight into the nature and origin of the gas. Here we present the deepest search to date for five molecules other than CO in the debris disk around 49 Ceti. 49 Ceti is a 40 Myr (Zuckerman & Song 2012) A-type star located 57.1 pc from Earth (Gaia Collaboration et al. 2018) that hosts one of the two brightest (in CO) and best-studied of the gas-bearing debris disks. The other system is β Pictoris, which has an almost identical CO(3-2) line flux at a factor of $\sim$3 closer distance (Matrà et al. 2017b). Despite their similar CO fluxes, 49 Ceti is a better candidate for a molecular line survey because its larger gas densities are more readily capable of exciting emission from higher critical density molecules, and its higher disk-averaged excitation temperature (32 K vs. 12 K in β Pic) is better for detecting lines with higher upper-level energies, thus implying

that we will get the strongest constraints on the molecular abundances. Its gas disk is also symmetric, unlike the β Pic disk, and covers a smaller solid angle on the sky, making it easier to spatially average the emission to maximize sensitivity from faint lines. Previous studies of the 49 Ceti system have spatially resolved the CO emission from the disk, revealing it to be axisymmetric and mostly consistent with Keplerian rotation about the central star between radii of $\sim$20 and $\sim$200 au (Hughes et al. 2008, 2017). There are hints of an anomalous (supersolar) C/O ratio from *Herschel* spectroscopy (Roberge et al. 2014), as well as evidence of active CO photodissociation with low H_2 abundances from the detection of strong CI emission (Higuchi et al. 2017b).

The five molecules selected for the search are CN, HCN, HCO^+, SiO, and CH_3OH. The low cross-section of CN to photodissociation makes it more likely to survive in the harsh radiation field of an A star, and in fact models of second-generation gas based on comets with Solar System abundances indicate that CN should be about as bright as, if not brighter than, CO (Matrà et al. 2018). It is also an excellent tracer of regions affected by UV radiation (Rodriguez-Franco et al. 1998), and seems to be enhanced in evolved protoplanetary disks (Kastner et al. 2014). CN is the daughter product of HCN photodissociation. HCN tends to be bright in both protoplanetary disks and comets (Biver et al. 2002; Öberg et al. 2010), although intriguingly it was not detected in previous, less-sensitive ALMA observations of the 49 Ceti system (Hughes et al. 2017). HCO^+ is similarly bright in both disks and comets (Guilloteau et al. 2016; Biver et al. 1997), and tends to be produced in regions where water has been photodissociated (Milam et al. 2004). It is also a sensitive tracer of ionization conditions in protoplanetary disks (Cleeves et al. 2015). While SiO has never been detected at millimeter wavelengths in protoplanetary disks or comets, it would provide unequivocal evidence for grain-grain collisions as the source of the gas. Methanol (CH_3OH) can be as abundant as CO in comets (Bockelée-Morvan et al. 2004; Mumma & Charnley 2011), but has only been detected once at a very low level in the nearest protoplanetary disk (Walsh et al. 2016) and in an outbursting young star (van 't Hoff et al. 2018).

In Section 2 we present the ALMA observations, and in Section 3 we describe the stringent upper limits we are able to place on the flux of all five molecules. In Section 4 we apply a spectral shifting technique pioneered by Matrà et al. (2017b) and similar to that of (Yen et al. 2016) that takes advantage of the known CO velocity

field to maximize any signal present in the noisy data. We then discuss our results in the context of known and predicted molecular abundances for protoplanetary disks, comets, and second-generation gas in Section 5, and summarize our conclusions in Section 6.

2. OBSERVATIONS

The observations (2017.1.00941.S, PI Hughes) utilized 48 of the 12-meter ALMA antennas in the most compact configuration available during Cycle 5. We observed using two spectral setups in Band 7, each executed on two separate dates. On 2018 June 2 and June 6, the spectral setup targeted HCN(4-3) at a rest frequency of 354.5 GHz, CH_3OH 1(1,1)-0(0,0) at a rest frequency of 350.9 GHz and several hyperfine transitions of CN(3-2) with the strongest at a rest frequency of 340.2 GHz. The other spectral setup observed on 2018 June 9 and 21 targeted SiO(8-7) at a rest frequency of 347.3 GHz, CH_3OH 4(1,3)-3(0,3) at a rest frequency of 358.6 GHz and HCO^+(4-3) at a rest frequency of 356.7 GHz. The three spectral windows targeting line emission used a spectral resolution of 976 kHz ($0.8 \, \mathrm{km \, s^{-1}}$) and bandwidth 1.875 GHz to maximize continuum sensitivity. One spectral window in each setup was configured for continuum observations (at frequencies of 341.5 and 345.3 GHz), with a bandwidth of 1.875 GHz and channel widths of 31.250 MHz ($27.5 \, \mathrm{km \, s^{-1}}$). The total on-source time was 1.6 hours per setup.

Table 1 gives the basic observational parameters for both spectral setups and all observing dates, including the number of antennas, time on source, naturally weighted beam size ("), the coordinates of the phase center in RA and Dec, bandpass calibrators, flux calibrators, and gain calibrators. Table 3 lists the rest frequency of each line (note that some were offset from the central frequency of the spectral window to satisfy constraints on the independently tunable intermediate frequencies (IFs).

The raw data were calibrated via the ALMA pipeline using the Common Astronomy Software Applications Package (CASA; McMullin et al. 2007) version 5.5.0-149. We used the CASA task `cvel` to convert the velocity axis from topocentric rest frame to the Kinematic Local Standard of Rest (LSRK). We used `UVCONTSUB` to fit a constant (a zeroth order polynomial) to channels more than $50 \, \mathrm{km \, s^{-1}}$ away from the known systemic velocity so that we could subtract the continuum. We used `TCLEAN` with natural weighting to produce channel maps for each molecule centered at the $2.78 \, \mathrm{km \, s^{-1}}$ LSR systemic velocity of the 49 Ceti system (Hughes et al. 2017) with pixel size $0\rlap{.}{''}15$ covering an area $22\rlap{.}{''}5 \times 22\rlap{.}{''}5$ on the sky.

Table 1. 49 Ceti Observational Parameters

# Antennas	48
Baseline distance	12 - 250 m
Time on Source	3.2 h[a]
Naturally Weighted Beam Size	$1\rlap{.}''1$ x $0\rlap{.}''9$
Phase center α	01:34:37.900573
Phase center δ	-15:40:34.94661

Dates	Bandpass Calibrator	Flux Calibrator	Gain Calibrator
02-Jun-2018	J0006-0623	J0006-0623	J0116-1136
06-Jun-2018	J0006-0623	J0006-0623	J0116-1136
09-Jun-2018	J0006-0623	J0141-0928	J0423-0120
21-Jun-2018	J0423-0120	J0423-0120	J0141-0928

[a]Divided into 1.6 h per spectral setup

3. RESULTS

We begin to search for emission from the five molecules by using the channel maps and zeroth-moment (velocity-integrated intensity) maps generated from the visibilities. We use the CASA task `immoments` to generate the moment 0 map, integrating channels within $\pm 5\,\mathrm{km\,s^{-1}}$ of the systemic velocity to ensure that all emission within the $8\,\mathrm{km\,s^{-1}}$ FWHM of the CO line (Hughes et al. 2008) is incorporated. The moment 0 maps are displayed in Figure 1 and show no significant gas emission.

CH$_3$OH and CN have multiple transitions in their spectral windows. CH$_3$OH has two transitions, 1(1,1)-0(0,0) and 4(1,3)-3(0,3), in two different spectral windows. CN exhibits many different hyperfine transitions within the same spectral window, all of which are listed in Table 2. For our initial reconnaissance, we shifted all of the hyperfine lines to a common velocity channel and added them together in both the disk-integrated, shifted spectra produced from the channel maps (see Section 4 for details), and in the moment 0 map, but did not detect any emission. For all subsequent analyses, we generate channel maps, spectra, and moment 0 maps for each methanol transition separately, and only for the strongest (highest intensity) of the CN transitions.

4. ANALYSIS

To obtain the most sensitive upper limits on the flux density of the molecules, we utilize a spatial-spectral shifting technique pioneered by Matrà et al. (2017a).
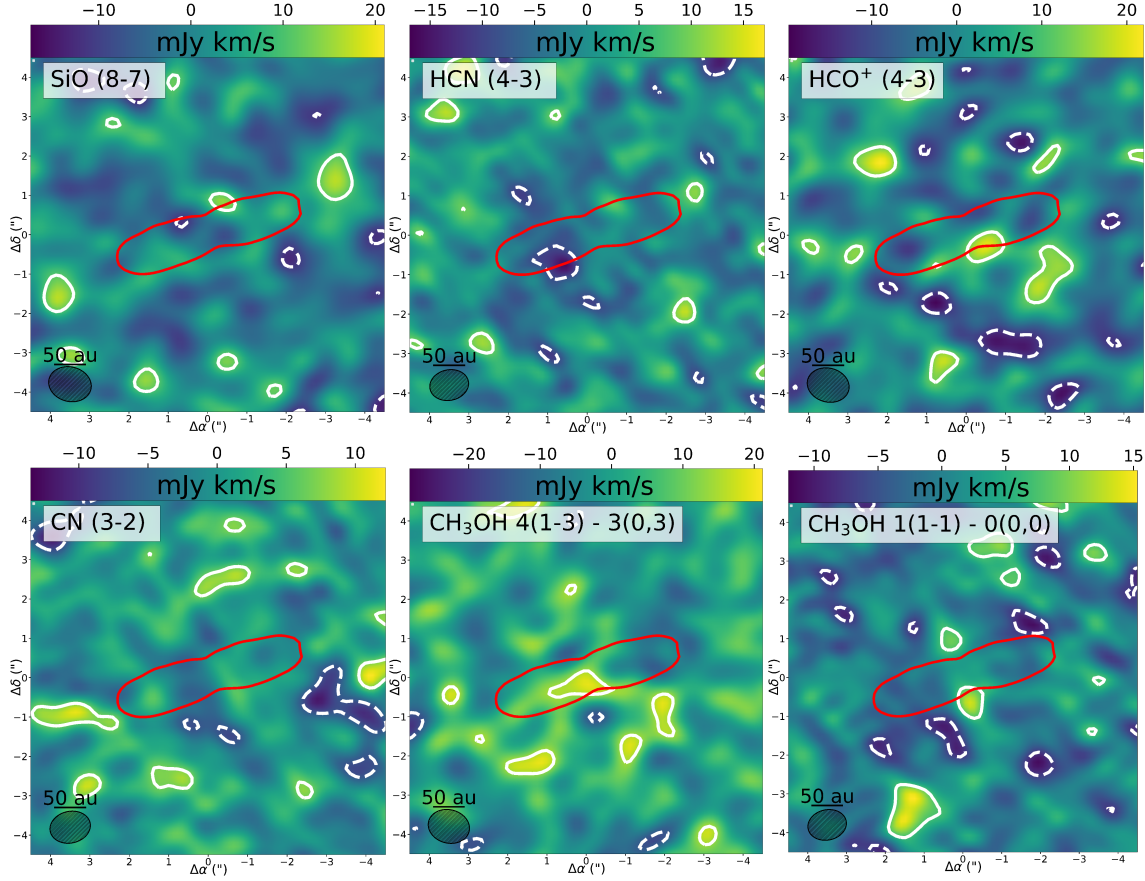
Figure 1.   Moment 0 maps for all six molecular lines in the survey, integrated within $\pm 5\,\mathrm{km\,s^{-1}}$ of the $2.78\,\mathrm{km\,s^{-1}}$ systemic velocity of 49 Ceti. The naturally weighted beam is indicated by the hatched ellipse located on the bottom left, below a 50 au scale bar. The red contour is an overlay of the CO(3-2) moment 0 map, indicating the spatial extent of the molecular line emission from the disk. The white contours are $\pm 2\sigma$, where σ is the rms noise in the image: 4.6, 5.5, 6.4, 7.2, 3.7, and $3.4\,\mathrm{mJy\,km\,s^{-1}\,beam^{-1}}$, for HCN(4-3), SiO(8-7), HCO$^+$(4-3), CH$_3$OH 4(1,3)-3(0,3), CH$_3$OH 1(1,1)-0(0,0), and CN(3-2), respectively. There is no statistically significant emission evident in any of the moment 0 maps.

The original technique uses a model velocity field to identify the expected location of flux within the 3-D position-position-velocity cube and shift the expected peak of the spectrum of each spatial pixel to a common velocity, thereby concentrating signal in a few channels. This technique substantially increases the signal-to-noise ratio (by concentrating signal rather than changing the noise level), as evidenced by

Table 2. CN Hyperfine Transitions

Rest Frequency[a] (GHz)	Transition	CDMS/Lovas Intensity[a]
339.44677	N= 3-2, J=5/2-5/2, F=3/2-3/2	-3.674
339.45999	N= 3-2, J=5/2-5/2, F=3/2-5/2	-4.3924
339.46263	N= 3-2, J=5/2-5/2, F=5/2-3/2	-4.3831
339.47590	N= 3-2, J=5/2-5/2, F=5/2-5/2	-3.5256
339.49321	N= 3-2, J=5/2-5/2, F=5/2-7/2	-4.3777
339.49928	N= 3-2, J=5/2-5/2, F=7/2-5/2	-4.3598
339.51663	N= 3-2, J=5/2-5/2, F=7/2-7/2	-3.3239
339.99225	N= 3-2, J=5/2-3/2, F=3/2-5/2	-4.4392
340.00809	N= 3-2, J=5/2-3/2, F=5/2-5/2	-3.0613
340.01960	N= 3-2, J=5/2-3/2, F=3/2-3/2	-3.0625
340.03154	N= 3-2, J=5/2-3/2, F=7/2-5/2	-2.1437
340.03540	N= 3-2, J=5/2-3/2, F=3/2-1/2	-2.5692
340.03540	N= 3-2, J=5/2-3/2, F=5/2-3/2	-2.3442
340.03540	N= 3-2, J=5/2-3/2, F=3/2-1/2	-2.5692
340.03540	N= 3-2, J=5/2-3/2, F=5/2-3/2	-2.3442
340.24777	N= 3-2, J=7/2-5/2, F=7/2-5/2	-2.1495
340.24777*	N= 3-2, J=7/2-5/2, F=9/2-7/2	-2.0159
340.24854	N= 3-2, J=7/2-5/2, F=5/2-3/2	-2.2887
340.26177	N= 3-2, J=7/2-5/2, F=5/2-5/2	-3.2027
340.26494	N= 3-2, J=7/2-5/2, F=7/2-7/2	-3.2039
340.27912	N= 3-2, J=7/2-5/2, F=5/2-7/2	-4.8867

* strongest transition

[a]https://www.cv.nrao.edu/php/splat/

the detection of a small quantity of CO in the disk around Fomalhaut that was not evident in the unprocessed channel or moment 0 maps (Matrà et al. 2017a).

We modify the technique slightly to utilize an observed velocity field rather than a model of a flat Keplerian disk. Previous observations of the 49 Ceti disk have demonstrated that 80% of the CO(3-2) flux is well described by an axisymmetric power-law disk in Keplerian rotation (Hughes et al. 2017), although the remaining 20% of the flux shows intriguing deviations from axisymmetry. We therefore use the moment 1 map of the CO(3-2) emission as the "model" velocity field, and shift each pixel according to the intensity-weighted velocity of CO at that location. Applying the method to the CO(3-2) data cube boosts the signal-to-noise ratio of the line by

a factor of 2-3 over a flat Keplerian model for 49 Ceti (Lambros 2018), although extending that result to the current data relies on the assumption that the targeted molecules share a common spatial distribution and velocity field with CO. Figure 2 shows the CO(3-2) moment 1 map generated from the data in Hughes et al. (2017), using the CASA task `immoments` and excluding pixels below three times the rms noise.
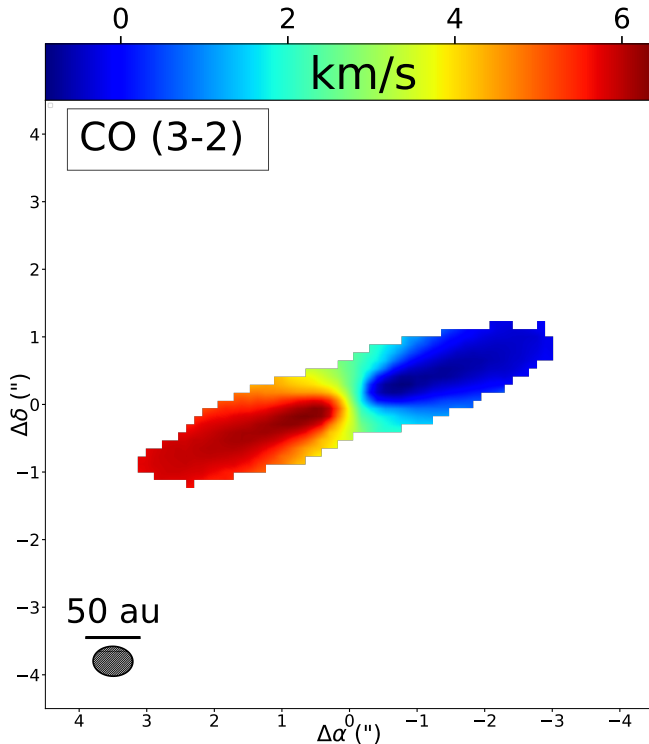

Figure 2. A moment 1 map of CO(3-2) in the 49 Ceti debris disk generated from data presented in Hughes et al. (2017). We use this observed intensity-weighted velocity field as the input for the spectral shifting technique drawn from Matrà et al. (2017a).

We applied this technique to our five molecules, subtracting the observed CO(3-2) gas velocity from the spectrum of each molecule in each pixel to shift any flux to a common zero-velocity channel. We then use the MIRIAD[1] task `cgcurs` to integrate the flux within the mask defined by the 3σ contours of the CO(3-2) moment 0 map. For molecules with multiple transitions (i.e., the CN hyperfine transitions

[1] Multichannel Image Reconstruction, Image Analysis and Display; (Sault et al. 1995)

listed in Table 2 and the two methanol transitions), we initially combined all the transitions by independently shifting and then subsequently adding together the 3-D position-position velocity cube for each transition before integrating the spectrum; however since no emission was detected we ultimately reported the upper limit for only the strongest transition in each spectral window. The resulting shifted spectra for all molecules are displayed in Figure 3. None of the spectra exhibit statistically significant $(> 3\sigma)$ emission near the expected velocity.

Table 3 lists the 3σ upper limit on the integrated flux for each line, calculated within the area enclosed by the 3σ contours of the shifted CO moment 0 map and integrated over $\pm 2.0\,\mathrm{km\,s^{-1}}$ along the velocity axis. We restrict the velocity to this range because Lambros (2018) demonstrated that applying the spectral shifting technique to the CO data from 49 Ceti narrowed the line considerably from its original $8\,\mathrm{km\,s^{-1}}$ width, but that a range of $\pm 2\,\mathrm{km\,s^{-1}}$ was still required to detect all of the shifted flux. The upper limit is calculated by measuring the rms noise in the moment 0 map, multiplying by the square root of the number of synthesized beams enclosed within the 3σ contours of the shifted CO moment map (the area within which the integrated flux is measured), and then multiplying by three to obtain the 3σ upper limit.

Table 3. Upper limits (3σ) on molecular gas emission from the 49 Ceti disk

Species	Rest Frequency[a] GHz	Upper Limit $\mathrm{mJy\,km\,s^{-1}}$	Gas Mass $M_\oplus$
CN(3-2)	340.248*	25	$<2.0 \times 10^{-8}$
SiO(8-7)	347.3305	34	$<8.3 \times 10^{-9}$
HCN(4-3)	354.5054	31	$<1.7 \times 10^{-9}$
HCO$^+$(4-3)	356.7342	37	$<1.3 \times 10^{-9}$
CH$_3$OH **	350.9051	22	$<1.5 \times 10^{-7}$
CH$_3$OH ***	358.6058	56	$<7.6 \times 10^{-7}$
*N=3-2, J=7/2-5/2, F=9/2-7/2 **1(1,1)-0(0,0) ***4(1,3)-3(0,3)			

[a]https://www.cv.nrao.edu/php/splat/

Even with the signal boost from the spatial-spectral shifting technique, we do not detect any gas emission from the five molecules. We convert the flux upper limits (calculated based on the noise level in the shifted moment 0 maps with the
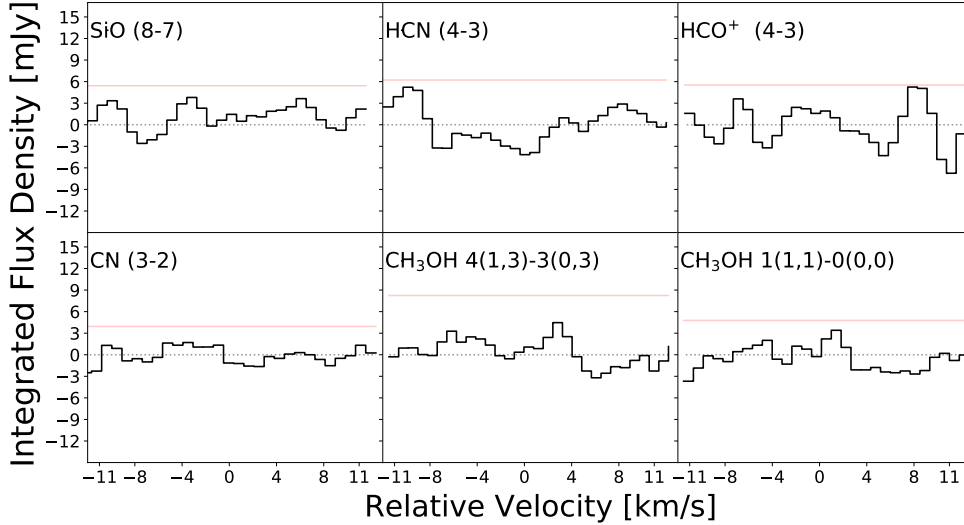
Figure 3. The shifted spectra for all five targeted molecules in the 49 Ceti system. The x-axis shows the velocity relative to the LSR velocity of 49 Ceti (so that $0\,\mathrm{km\,s^{-1}}$ is the expected velocity of the emission). Each spectrum was created utilizing the shifted channel maps, which were then integrated over the area of the disk enclosed by the 3σ contours of the CO(3-2) moment 0 map. The CN spectrum shows only the strongest (highest intensity) of the hyperfine transitions. The red horizontal line denotes the 3σ flux level for each spectrum (three times the rms noise for the spectrum, calculated across at least 100 channels around the line within each spectral window). There is no significant ($> 3\sigma$) emission near a velocity of $0\,\mathrm{km\,s^{-1}}$ for any of the observed lines.

velocity range restricted to $\pm 2\,\mathrm{km\,s^{-1}}$) to mass upper limits, assuming optically thin emission and local thermodynamic equilibrium (LTE) and adopting the disk-averaged excitation temperature of $\mathrm{T_{ex}} = 32\,\mathrm{K}$ from the CO line ratio in Hughes et al. (2017), using the following relationships:

$$M = \frac{4\pi}{h\nu_0}\frac{F_{J_u - J_l}\mathrm{m}_{mol}\mathrm{d}^2}{A_{J_u - J_l}X_u} \tag{1}$$

$$X_u = \frac{g_u}{Q(T)}e^{-E_u/kT_{ex}} \tag{2}$$

where m_{mol} is the molecular mass, d is the distance to the source, ν_0 is the rest frequency for each transition taken from the Splatalogue database, $A_{J_u - J_l}$ is the Einstein

coefficient (also taken from Splatalogue), X_u represents the fraction of molecules in the upper energy state, and $F_{J_u-J_l}$ is the upper limit on the flux density for a given transition from Table 3. The mass of each molecule, m_{mol}, the degeneracy of the upper state g_u, the energy of the upper state E_u, and the tabulated partition function at a temperature of 37.5K (the closest to our assumed excitation temperature) $Q(T)$, were taken from the Cologne Database for Molecular Spectroscopy (CDMS). Table 4 summarizes the parameters for each molecule, and Table 3 lists the corresponding upper limit on the gas mass of each molecule.

Table 4. Molecular Parameters

Species	Mass (Da)	A $(\mathrm{s}^{-1})^a$ (mJy km s^{-1})	E_u (cm$^{-1})^b$	g_u^b	Q(T)^b
CN	26.00362^b	4.1313×10^{-4}	22.7028	10	84.7308
SiO	43.97184^b	2.2030×10^{-3}	52.1397	17	36.3268
HCN	27.01090^a	2.0605×10^{-3}	29.5633	27	53.9106
HCO$^+$	29.00274^c	3.5722×10^{-3}	29.7491	9	17.8601
CH$_3$OH	32.02622^b	3.3148×10^{-4}	11.7049	12	920.963739
CH$_3$OH	32.02622^b	1.3193×10^{-4}	30.7644	36	920.963739

[b] www.chemspider.com

[c] cdms.astro.uni-koeln.de (Endres et al. 2016)

[d] Kim et al. (2018)

5. DISCUSSION

To date, CO remains the only firmly detected gas-phase molecule in debris disks (Hughes et al. 2018). The upper limit on HCN(4-3) from our line survey is deeper than a previous search for HCN in the 49 Ceti disk (Hughes et al. 2017), by a factor of about 2.5 in rms noise, which is enhanced to $\sim 5\times$ by our use of the spectral shifting technique. Matrà et al. (2018) conducted a Submillimeter Array (SMA) and ALMA survey for CN, HCN, HCO$^+$, N$_2$H$^+$, H$_2$CO, H$_2$S, CH$_3$OH, SiO, and DCN in the β Pic disk that also returned upper limits. When applying a simple scaling relationship for the differences in distance, frequency, and Einstein coefficient to the flux upper limits, our survey is roughly 7–$13\times$ more sensitive to CN, HCN, HCO$^+$, and methanol. The emerging picture seems to be that the abundance of molecules other than CO is surprisingly low in debris disks, even for those molecules that exhibit relatively high abundances in (1) protoplanetary disks, (2) solar system comets, and (3) models of secondary gas emission. Here we explore how the gas composition implied by our upper limits compares with the abundance ratios of those three categories of objects.

5.1. *Comparison with Observed Molecular Abundances of Protoplanetary Disks and Comets*

Protoplanetary disks exhibit a rich chemistry that has been studied both observationally and theoretically, with the field undergoing a particularly rapid expansion recently as ALMA has reached maturity (Henning & Semenov 2013; Dutrey et al. 2014; Bergin & Cleeves 2018). All of the molecules in our survey, with the exception of SiO, have been detected in one or more protoplanetary disks.

Models of protoplanetary disk chemistry predict a rich abundance of molecular species, as a result of stellar and interstellar radiation, cosmic rays, and grain surface chemistry (e.g., Aikawa & Herbst 1999; Aikawa et al. 1999). HCO$^+$ and HCN are particularly abundant, both in the models and subsequent observations. In a survey of eight T Tauri disks and four Herbig Ae disks with the SMA, HCO$^+$(3-2) emission was detected towards all of the surveyed objects and HCN(3-2) was at least tentatively detected towards 10 of the 12 sources (Öberg et al. 2010, 2011). Typical rms noise levels in the survey were of order $\sim 0.1\,\mathrm{Jy\,km\,s^{-1}}$ at distances of $\sim$140 pc (although V4046 Sgr was closer). If we scale those thresholds by ν^2 (assuming optically thick emission) and by d^2 to account for the difference in distance to the 49 Ceti

system, then our upper limits on the integrated HCO$^+$(4-3) and HCN(4-3) flux from 49 Ceti are about a factor of 50 below the sensitivity of the Öberg et al. (2010, 2011) survey. The CO(2-1) emission from 49 Ceti (3.87 ± 0.41 Jy km s^{-1}, Moór et al. 2019) is 26 times lower than the average for the disks in the Öberg et al. (2011) survey, and 10 times lower than the faintest disk in the survey. Looking at it another way, the ratio of HCO$^+$/CO flux within a given band varies in the Öberg et al. (2010, 2011) sample between 0.11 and 0.59, while the ratio for 49 Ceti at Band 7 is < 0.006. HCN is less conclusive, since there are two upper limits within the sample of 12, but for sources in which it is detected the HCN/CO ratio ranges from 2.0 to 18, while the ratio for 49 Ceti is < 0.005. A protoplanetary composition for the 49 Ceti disk is not supported by the low limits on both HCO$^+$ and HCN compared to CO emission.

The nondetections of CH$_3$OH and CN are less relevant for comparison with a protoplanetary disk composition. While Walsh et al. (2014) predicted detectable CH$_3$OH emission from protoplanetary disks based on models of grain-surface chemistry, nonthermal desorption, and irradiation of grain mantles, subsequent observations yielded lower abundances than expected by two orders of magnitude (Walsh et al. 2016). Observations of the nearest and brightest Herbig Ae disk (around HD 163296) have demonstrated an even lower CH$_3$OH/H$_2$CO ratio than in the TW Hya system (the closest protoplanetary disk and the only non-outbursting source in which methanol has been detected to date), suggesting that abundances may be suppressed even further in the radiation field of an A star. We therefore would not expect to detect CH$_3$OH in the 49 Ceti system even if its abundance relative to CO were protoplanetary. Similarly, a recent ALMA survey of molecular lines from protoplanetary disks in Lupus returned detections of CN(3-2) in only 38% of surveyed sources (van Terwisga et al. 2019). Typical upper limits were of order ~ 100 mJy km s^{-1}, however, which is about a factor of 30 above our upper limits when scaled to the appropriate distance. This result is similar to previous surveys showing that $\sim$50% of bright protoplanetary disks exhibit detectable CN at modest sensitivity (e.g., Guilloteau et al. 2013). Our nondetection of CN is therefore inconclusive as a probe of protoplanetary composition.

Solar system comets serve as a foundation for predicting the likely composition of second-generation gas in extrasolar systems, although they are imperfect comparison objects for many reasons – foremost that most Solar System comets are observed while sublimating at distances of a few au from the Sun, whereas the gas in extra-

solar debris disks originates from tens to hundreds of au from the central star. The radiation field of an A star differs markedly from that of the Sun, and the mechanism behind the gas release may differ as well (collisional vs. radiative).

In a millimeter-wavelength survey of the composition of 24 comets with the Institut de Radioastronomie Millimetrique 30m, James Clerk Maxwell Telecope, Caltech Submillimeter Observatory, and Swedish-ESO Submillimeter Telescope, HCN was detected in all 24 comets with an abundance relative to CO of order $\sim$0.1-1 (Biver et al. 2002). HCN lines in this survey were typically as bright or brighter than the CO lines observed in the same band. These compositional relationships are also borne out across larger and more modern samples of comets (Mumma & Charnley 2011; Bockelée-Morvan & Biver 2017). In the 49 Ceti system, the HCN(4-3) upper limit of $31\,\mathrm{mJy\,km\,s^{-1}}$ from this work implies an HCN(4-3)/CO(3-2) line ratio of < 0.0052, using the CO(3-2) flux of $6.0 \pm 0.1\,\mathrm{Jy\,km\,s^{-1}}$ from Hughes et al. (2017). This limit is well below the observed range of HCN(4-3)/CO(3-2) line ratios for Solar System comets, which span values of $\sim$1-20, although for most systems CO was not detected at all with lower limits of order $\gtrsim 10$ (Biver et al. 2002, and references therein). HCO$^+$ has also been detected in comets and may be particularly prevalent in regions where water has been photodissociated (Milam et al. 2004). If the 49 Ceti disk exhibited the same abundance patters as Solar System comets, we would therefore strongly expect to detect HCN, and would likely detect methanol and HCO$^+$. The lack of detection of any of these molecules suggests that we need to dig deeper into modeling of second-generation gas to understand why the abundance ratios indicated by our observations differ so markedly from *both* protoplanetary disks and comets.

5.2. *Models of Second-Generation Gas Production*

In this section we explore models of second-generation gas production, beginning with an estimate of the CO photodissociation and survival timescale assuming only shielding by H_2 and self-shielding by CO (Section 5.2.1). We then extend the analysis to CN, which is the molecule in our survey that has the best combination of a long survival timescale against photodissociation and intrinsically strong molecular transitions (Section 5.2.2). Finally, we derive constraints on the HCN/(CO+CO$_2$) outgassing rate ratios (Section 5.2.3). The latter two sections follow the methodology derived in Matrà et al. (2018), applying it to these new and more stringent constraints for the specific case of the 49 Ceti system.

5.2.1. *CO photodissociation and survival timescale*

As ALMA has matured and detections of gas in debris disks have started piling up (e.g., Zuckerman et al. 1995; Moór et al. 2011, 2015, 2017; Dent et al. 2014; Greaves et al. 2016; Lieman-Sifry et al. 2016; Marino et al. 2016, 2017; Matrà et al. 2017a), there have been a number of advances in models of second-generation gas production in debris disks. There are several proposed mechanisms, including collisional gas release (Zuckerman & Song 2012; Dent et al. 2014), thermal desorption (Czechowski & Mann 2007), and photodesorption (Grigorieva et al. 2007). Recent modeling efforts have primarily focused on collisional gas release from icy planetesimals as the origin of the outgassing responsible for the observed molecular lines (Matrà et al. 2017b; Kral et al. 2017). In this section we apply the model presented in Matrà et al. (2017b) to our observations of the 49 Ceti disk to investigate the origin of the gas.

We first estimate the photodissociation timescale for CO using models of the temperature and density structure of the CO disk presented in Hughes et al. (2017). We calculate half the vertical column density through the disk. We perform this calculation for both scenarios investigated in the paper: a primordial scenario in which the CO/H_2 abundance is assumed to equal 10^{-4}, and a second-generation scenario in which the CO/H_2 abundance is assumed to equal 1. We also scale up the mass of the Hughes et al. (2017) best-fit models to match the total CO mass of $(1.11 \pm 0.13) \times 10^{-2}$ $M_\oplus$ derived by Moór et al. (2019). In the primordial scenario (where the gas is in LTE) the CO column density is 2.0×10^{16} cm^{-2} and the H_2 column density is 2.0×10^{20} cm^{-2}, whereas in the second-generation scenario (where the conditions are non-LTE), both CO and H_2 have column densities of 3.6×10^{16} cm^{-2}.

Since the dust in the 49 Ceti system is optically thin, we assume negligible dust attenuation. We then estimate the photodissociation timescale using the following relationships, following Flaherty et al. (2019):

$$k = \chi k_0 \Theta e^{-\gamma A_v} \tag{3}$$

$$t = 1/k \tag{4}$$

In these equations, χ is the radiation field in units of the Draine field (one Draine field is $\sim$1.7 Habings, where a Habing is 1.6×10^{-3} erg cm^{-2} s^{-1}; Draine 1978). We consider only the interstellar radiation field (ISRF), and ignore contributions from the stellar radiation field (which would only decrease the photodissociation timescale). k_0 is the unattenuated photodissociation rate in units of photodissociations per second for CO

molecules. We used $k_0 = 2.590 \times 10^{-10}\,\text{s}^{-1}$ from Table 6 of Visser et al. (2009), since Table 6 assumes an excitation temperature of $50\,\text{K}$ which is closest to the disk-averaged excitation temperature of $32\,\text{K}$ derived by Hughes et al. (2017). Θ is the attenuation factor for self-shielding and H_2 shielding, tabulated in (Visser et al. 2009) for different values of CO and H_2 column density. γ is the UV extinction relative to visual extinction (≈ 2 for small dust grains). The photodissociation timescale is then $1/k$. We consider the simple case with no dust attenuation throughout the disk ($A_V = 0$), using the value of Θ corresponding to the column density, which amounts to an assumption that the photodissociation timescale is set by the most heavily shielded molecules in the disk (Visser et al. 2009). We calculate a photodissociation timescale of $\sim$6,000 yr for the primordial scenario and $\sim$3,300 yr for the second-generation case (due to the differences in column density, which correspond to different values of Θ). These timescales should be considered upper limits, since we have neglected stellar radiation, which could contribute up to the same amount of radiation as the ISRF depending on the optical thickness of the radial gas column.

These results present a familiar dilemma: the photodissociation timescale is so short compared to the age of the star that a primordial origin for the gas is unlikely, but the combination of large CO mass and short photodissociation timescale requires an uncomfortably high gas release rate from large bodies to sustain the observed gas (see, e.g., Kóspál et al. 2013). Recent work by Kral et al. (2019) suggests that the solution to the dilemma may lie in shielding of CO by neutral carbon in the disk, which is not included in the standard calculation of the photodissociation timescale that we performed, but which can extend the lifetime of CO by orders of magnitude. Observations by Higuchi et al. (2017a) demonstrated substantial reservoirs of neutral carbon in the disk, as expected due to rapid initial photodissociation of CO, and a detailed analysis by Moór et al. (2019) demonstrated that the amount of CO is consistent with the Kral et al. (2019) model given the observed quantity of CI in the 49 Ceti system. These results provide evidence for a secondary origin for CO in the disk. They are supported by the unresolved vertical height of the CO disk, which is smaller than expected for a primordial composition and implies a mean molecular weight more consistent with CO (rather than H_2) as the dominant constituent (Hughes et al. 2017). However, it is worth noting that the long photodissociation timescale of CO implied by CI shielding would apply equally to CO of primordial or secondary origin.

5.2.2. *CN photodissociation, mass, and survival timescale*

While the LTE estimates provide a ballpark value for the conversions between flux and mass, if the H_2 density is low, then it is likely that at least some species are not in LTE. Moving on to molecules other than CO, we can convert the upper limits in our survey to gas masses via the non-LTE calculation described in Matrà et al. (2018). We focus on CN, since for Solar System comet-like compositions it is expected to be the most favourable for mm-wave detection (Matrà et al. 2018), compared to other molecules expected in a cometary environment (like the observed CH_3OH and HCN). This is largely due to CN having the best combination of a long survival timescale against photodissociation, and intrinsically strong molecular transitions. We do not consider SiO gas as we are not aware of its detection in Solar System comets, and HCO^+ because connecting its gas mass to parent species in exocometary ice would depend on a complex network involving chemistry and ionization balance, which is beyond the scope of this paper.

We begin by converting the upper limit on the CN flux of $25\,\mathrm{mJy\,km\,s^{-1}}$ to a mass upper limit using Eq. 2 from Matrà et al. (2015). This calculation assumes that any CN emission at millimeter wavelengths is optically thin, which we will verify *a posteriori*. To calculate the excitation of the molecule and hence the upper level fractional population, x_j, we use the NLTE code developed in the same paper, where x_j will depend on the density of collisional partners (e.g., electrons) and the gas kinetic temperature, T_k. Fig. 4 (top panel) shows the derived total CN masses from the measured upper limit as a function of collider density and temperature. The excitation calculation includes fluorescence due to absorption of stellar and interstellar optical/UV photons and later re-emission at lower-energy transitions (Matrà et al. 2018). For the stellar radiation field, we assume a PHOENIX stellar model with $T_{\mathrm{eff}}=8800\,\mathrm{K}$, $R_*=1.7\,\mathrm{R_\odot}$, $\log(g) = 4.0$, $[M/H] = 0.06$ (G. Kennedy, private communication), and scaled its flux to what would be received by a CN molecule at $140\,\mathrm{au}$. This analysis leads to mass upper limits ranging between $(6.2\text{-}23)\times10^{-9}\,\mathrm{M_\oplus}$.

We then check whether the resulting emission is optically thin along the line of sight to Earth. We rescale the CO radial column density from the secondary gas model of Hughes et al. (2017) (measured from the star to the disk's critical radius, and multiplied by two to account for the entire radial extent of the disk) by the CN/CO total abundance ratio to get the CN radial column density, which we assume is comparable to the column density of CN along the line of sight to Earth. These
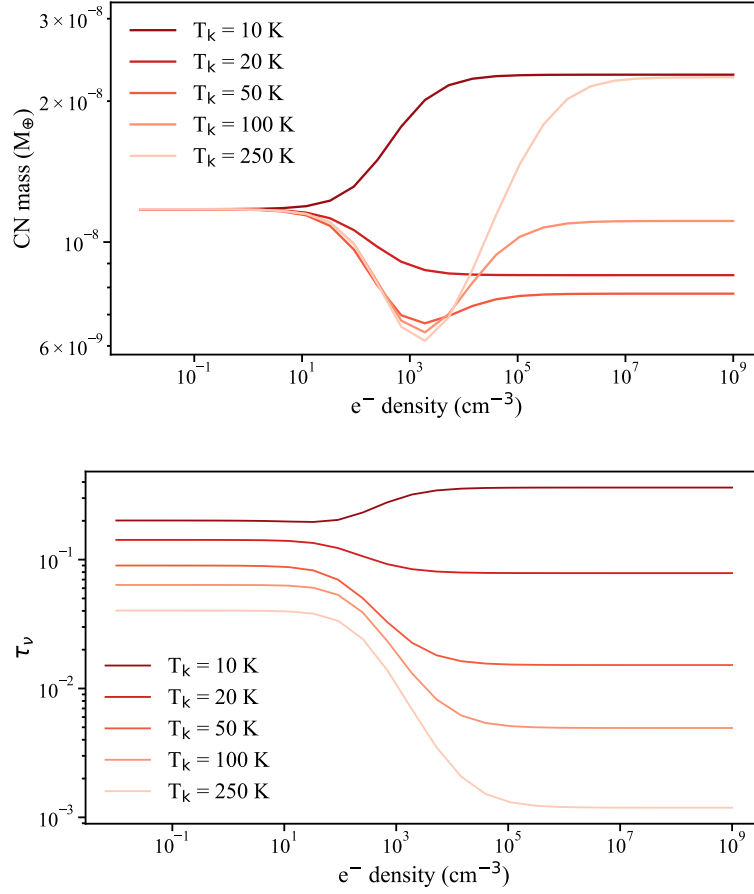
Figure 4. (Top) Total CN mass as a function of collider density (with primary collider assumed to be electrons) and kinetic temperature. The total mass of CN from these models is $(6.2-23)\times10^{-9}\,\mathrm{M}_\oplus$. (Bottom) Optical depth as a function of collider density and kinetic temperature. In order to check the assumption that CN was optically thin in the debris disk, the calculated CO column densities through the disk midplane were re-scaled by the CN/CO total mass ratio to obtain a CN column density. This was then turned into an optical depth using Eq. 3 in Matrà et al. (2017b).

assumptions result in CN column densities of $(1.0\text{-}3.9)\times10^{12}\,\mathrm{cm}^{-2}$, depending on excitation, which (via Eq. 3 in Matrà et al. (2017b), assuming line widths produced by thermal broadening by T_K) lead to optical depths of 0.001-0.36 (bottom panel of Fig. 4). Therefore, CN emission, even if just below our upper limit, would be largely optically thin. Note that this calculation does not account for uncertainties in the

amount of stellar radiation, or the radius at which it is received (140 au is assumed), or the distance to the star from Earth.

From there, we can investigate CN photodissociation. By rescaling the previously calculated CO column density along the vertical direction, we obtain CN column densities of $(2.2\text{-}8.0)\times10^{10}\,\mathrm{cm}^{-2}$, for which self-shielding is negligible[2]. The shielding factors due to CO, H_2, and CI column densities (taking CI/CO = 54 from Higuchi et al. 2017a) are $\sim$0.91, $\sim$0.98 and $\sim$0.43, giving a combined shielding factor of $\sim$0.38 (Heays et al. 2017). Note that the combined shielding factor is approximated as the product of the shielding factors of the individual species, which assumes that the wavelength regimes over which the shielding takes place do not overlap, but we consider this a reasonable approximation especially given the minor contributions from CO and H_2. Considering only the ISRF UV field impinging on the disk from the vertical direction, we obtain a photodissociation timescale for CN of order $\sim$161 years.

5.2.3. *Constraints on the HCN/(CO+CO$_2$) outgassing rate ratios*

If we assume that 1) all CN gas is produced by photodissociation of exocometary HCN gas, which is itself produced by cometary release of HCN ice; 2) all CO gas is produced by either cometary release of CO ice, or photodissociation of CO_2 released from CO_2 ice; and 3) that the production and destruction rates of each species are balanced (i.e., we are in steady state, although this is not necessarily the case in young systems, see Marino et al. (2020)), we can relate the observed CN and CO gas masses to the HCN/(CO+CO$_2$) outgassing rate ratio. From Eq. 3 in Matrà et al. (2018), this can be expressed as

$$\frac{M_{\mathrm{CN}}}{M_{\mathrm{CO}}} = \frac{\tau^-_{\mathrm{CN,phd}}m_{\mathrm{CN}}}{\tau^-_{\mathrm{CO,phd}}m_{\mathrm{CO}}} \frac{\dot{N}^+_{\mathrm{HCN}}}{\dot{N}^+_{\mathrm{CO+CO_2}}}, \tag{5}$$

where m_{i} is the molecular mass in kg, $\dot{N}^+_{\mathrm{i}}$ its production (outgassing) rate in number of molecules per second, M_{i} the observed gas mass, and τ^-_{i} its photodissociation timescale of the gas species.

The observed gas masses M_{CO} and M_{CN} are well constrained observationally from Moór et al. (2019) and our data, and the CN photodissociation timescale $\tau^-_{\mathrm{CN,phd}}$ is also relatively well constrained, as shielding only increases it by a factor of a few

---

[2] https://home.strw.leidenuniv.nl/∼ewine/photo/data/photo_data/line_shielding_functions/CN/photodissociation_ISRF

(Sect. 5.2.2). On the other hand, the main uncertainty in the calculation remains the CO photodissociation timescale $\tau^-_{CO,phd}$, which can range from a few hundred years if shielding by CI is neglected to much longer than the system age of 40 Myr.

Taking the CO photodissociation timescale $\tau^-_{CO,phd} \sim$3,300 yr derived in our second-generation, CI-free model would imply a HCN/(CO+CO$_2$) outgassing rate ratio of (1.2-4.6) $\times 10^{-5}$. This is at least a factor of $\sim$65 below the observed values for Solar system comets, ranging from about $3 \times 10^{-3} - 2$ (see Fig. 5 in Matrà et al. 2018). Therefore, in the absence of CI shielding the constraint on the flux density of CN and HCN implies that either CO may be preferentially released from the exocometary ice relative to HCN, or there may be a true HCN depletion compared to CO ice in 49 Ceti's exocomets.

Perhaps more likely, however, given the work of Kral et al. (2019) and the observed presence of CI, is that CI is preferentially shielding CO from UV photodissociation. For example, if we assume the CI/CO ratio of 54 derived from Higuchi et al. (2017a) (which does not account for optical depth and excitation effects) we obtain a CO shielding factor of $\sim 10^{-15}$. This is so small that it would imply that CO is hardly photodissociating at all, allowing it to survive for much longer than the age of the system. Shielding by CI has a much weaker effect on other molecules, since the CO photodissociation bands are all at wavelengths shorter than the CI ionization threshold (110 nm), whereas some photodissociation bands of CN (and those of most other cometary molecules) extend beyond 110 nm, where the stellar radiation field is orders of magnitude stronger.

It therefore seems likely that the only reason CO appears so anomalously abundant is due to shielding by CI, and that CN is in fact photodissociated about as rapidly as we would expect given the harsh UV radiation field from both the ISRF and the central A star. Whether CI shielding is the cause of the overabundance of CO compared to other molecules could be confirmed with an accurate measurement of the CI column density. This can be achieved with future high resolution, optically thin, multi-transition CI observations, which are best suited to solving the degeneracy between excitation, spatial structure, mass, and optical depth which affects single line measurements. If CI column densities are confirmed to be very high, then the CO photodissociation timescale $\tau^-_{CO,phd}$ in Eq. 5 could be orders of magnitude higher than derived in the absence of CI shielding, and allow us to reconcile our extreme

CN/CO flux ratios around 49 Ceti with Solar System comet -like $HCN/(CO+CO_2)$ ice abundances.

6. CONCLUSIONS

In order to constrain the composition of the gas in nearby debris disks, we performed a deep survey for five molecular species in the disk around 49 Ceti. After 3.2 hours of integration with ALMA at low angular and spectral resolution to maximize sensitivity, and after applying a spatial-spectral shifting technique adapted from Matrà et al. (2017a), we obtain stringent upper limits from the shifted and velocity-range-restricted moment 0 maps that represent the most sensitive search to date for molecules other than CO in a debris disk: HCN(4-3) at $31\,\mathrm{mJy\,km\,s^{-1}}$, HCO^+(4-3) at $37\,\mathrm{mJy\,km\,s^{-1}}$, CN(3-2) at $25\,\mathrm{mJy\,km\,s^{-1}}$, SiO(8-7) at $34\,\mathrm{mJy\,km\,s^{-1}}$, CH_3OH 1(1,1)-0(0,0) at $22\,\mathrm{mJy\,km\,s^{-1}}$, and CH_3OH 4(1,3)-3(0,3) at $56\,\mathrm{mJy\,km\,s^{-1}}$.

We use our upper limits on the flux density to calculate flux ratios that we can compare with the composition of protoplanetary disks and solar system comets. The upper limits on the HCN/CO and HCO^+/CO line ratios are inconsistent with a protoplanetary composition for the disk material. The upper limits on the HCN/CO ratio and the nondetection of HCO^+ and methanol are also inconsistent with the range of cometary compositions observed within the Solar System. Since the temperatures and mechanisms involved in the release of exocometary gas at tens to hundreds of au from the central star may differ markedly from those involved in the au-scale sublimation of Solar System comets, we turn to models of second-generation gas production to resolve this apparent conundrum. While the CO photodissociation timescale is apparently much shorter than the age of the system, it can be extended by orders of magnitude by taking into account shielding by CI (Kral et al. 2019), which is observed to be present in abundance in the 49 Ceti system, likely as a byproduct of CO photodissociation (Higuchi et al. 2017a). Using a NLTE code from Matrà et al. (2018), we demonstrate that if CI shielding is neglected, then the implied HCN/CO outgassing ratio for 49 Ceti would be orders of magnitude lower than the range observed for Solar System comets.

Our results imply that either there is a marked difference in the chemical abundance of the 49 Ceti system relative to all known Solar System comets and protoplanetary disks, an unspecified mechanism causing preferential release of CO relative to HCN, or more plausibly, that our results provide support for a picture where CI shields CO, but cannot shield CN and other (exo-)cometary molecules. The apparently high

abundance of CO relative to the other molecules therefore may not reflect the true chemical abundances of the icy bodies in the system, but rather reflects the fact that only CO is shielded from photodissociation and therefore accumulates in substantial amounts while the other molecules are photodissociated so rapidly as to be effectively invisible. Our deep limits on molecular species readily detected in protoplanetary disks and comets provide support for the shielding of CO by CI in the 49 Ceti system.

ACKNOWLEDGMENTS

REFERENCES

Aikawa, Y., & Herbst, E. 1999, A&A, 351, 233

Aikawa, Y., Umebayashi, T., Nakano, T., & Miyama, S. M. 1999, ApJ, 519, 705

Bergin, E. A., & Cleeves, L. I. 2018, Chemistry During the Gas-Rich Stage of Planet Formation, 137

Beust, H., Lagrange-Henri, A. M., Madjar, A. V., & Ferlet, R. 1990, A&A, 236, 202

Biver, N., Bockelee-Morvan, D., Colom, P., et al. 1997, Science, 275, 1915

Biver, N., Bockelée-Morvan, D., Crovisier, J., et al. 2002, Earth Moon and Planets, 90, 323

Bockelée-Morvan, D., & Biver, N. 2017, Philosophical Transactions of the Royal Society of London Series A, 375, 20160252

Bockelée-Morvan, D., Crovisier, J., Mumma, M. J., & Weaver, H. A. 2004, The composition of cometary volatiles (University of Arizona Press), 391

Cleeves, L. I., Bergin, E. A., Qi, C., Adams, F. C., & Öberg, K. I. 2015, ApJ, 799, 204

Czechowski, A., & Mann, I. 2007, ApJ, 660, 1541

Dent, W. R. F., Wyatt, M. C., Roberge, A., et al. 2014, Science, 343, 1490

Draine, B. T. 1978, ApJS, 36, 595

Dutrey, A., Semenov, D., Chapillon, E., et al. 2014, in Protostars and Planets VI, ed. H. Beuther, R. S. Klessen, C. P. Dullemond, & T. Henning, 317

Endres, C. P., Schlemmer, S., Schilke, P., Stutzki, J., & Müller, H. S. P. 2016, Journal of Molecular Spectroscopy, 327, 95

Flaherty, K., Hughes, A. M., Mamajek, E. E., & Murphy, S. J. 2019, ApJ, 872, 92

Gaia Collaboration, Mignard, F., Klioner, S. A., et al. 2018, A&A, 616, A14

Greaves, J. S., Holland, W. S., Matthews, B. C., et al. 2016, MNRAS, 461, 3910

Grigorieva, A., Thébault, P., Artymowicz, P., & Brand eker, A. 2007, A&A, 475, 755

Guilloteau, S., Di Folco, E., Dutrey, A., et al. 2013, A&A, 549, A92

Guilloteau, S., Reboussin, L., Dutrey, A., et al. 2016, A&A, 592, A124

Heays, A. N., Bosman, A. D., & van Dishoeck, E. F. 2017, A&A, 602, A105

Henning, T., & Semenov, D. 2013, Chemical Reviews, 113, 9016

Higuchi, A. E., Sato, A., Tsukagoshi, T., et al. 2017a, ApJ, 839, L14

—. 2017b, ApJ, 839, L14

Hughes, A. M., Duchêne, G., & Matthews, B. C. 2018, Annual Review of Astronomy and Astrophysics, 56, 541

Hughes, A. M., Wilner, D. J., Kamp, I., & Hogerheijde, M. R. 2008, ApJ, 681, 626

Hughes, A. M., Lieman-Sifry, J., Flaherty, K. M., et al. 2017, ApJ, 839, 86

Jackson, A. P., Wyatt, M. C., Bonsor, A., & Veras, D. 2014, MNRAS, 440, 3757

Kastner, J. H., Hily-Blant, P., Rodriguez, D. R., Punzi, K., & Forveille, T. 2014, ApJ, 793, 55

Kim, S., Chen, J., Cheng, T., et al. 2018, Nucleic Acids Research, 47, D1102. https://doi.org/10.1093/nar/gky1033

Kóspál, Á., Moór, A., Juhász, A., et al. 2013, ApJ, 776, 77

Kral, Q., Marino, S., Wyatt, M. C., Kama, M., & Matrà, L. 2019, MNRAS, 489, 3670

Kral, Q., Matrà, L., Wyatt, M. C., & Kennedy, G. M. 2017, MNRAS, 469, 521

Lambros, Z. 2018, Wesleyan University, Middletown, CT, USA

Lieman-Sifry, J., Hughes, A. M., Carpenter, J. M., et al. 2016, ApJ, 828, 25

Marino, S., Flock, M., Henning, T., et al. 2020, MNRAS, 492, 4409

Marino, S., Matrà, L., Stark, C., et al. 2016, MNRAS, 460, 2933

Marino, S., Wyatt, M. C., Panić, O., et al. 2017, MNRAS, 465, 2595

Matrà, L., Panić, O., Wyatt, M. C., & Dent, W. R. F. 2015, MNRAS, 447, 3936

Matrà, L., Wilner, D. J., Öberg, K. I., et al. 2018, ApJ, 853, 147

Matrà, L., MacGregor, M. A., Kalas, P., et al. 2017a, ApJ, 842, 9

Matrà, L., Dent, W. R. F., Wyatt, M. C., et al. 2017b, MNRAS, 464, 1415

Mckinney, W. 2010, Proceedings of the 9th Python in Science Conference

McMullin, J. P., Waters, B., Schiebel, D., Young, W., & Golap, K. 2007, in Astronomical Society of the Pacific Conference Series, Vol. 376, Astronomical Data Analysis Software and Systems XVI, ed. R. A. Shaw, F. Hill, & D. J. Bell, 127

Milam, S. N., Savage, C., Ziurys, L. M., & Wyckoff, S. 2004, ApJ, 615, 1054

Moór, A., Ábrahám, P., Juhász, A., et al. 2011, ApJ, 740, L7

Moór, A., Henning, T., Juhász, A., et al. 2015, ApJ, 814, 42

Moór, A., Curé, M., Kóspál, Á., et al. 2017, ApJ, 849, 123

Moór, A., Kral, Q., Ábrahám, P., et al. 2019, ApJ, 884, 108

Mumma, M. J., & Charnley, S. B. 2011, ARA&A, 49, 471

Öberg, K. I., Qi, C., Fogel, J. K. J., et al. 2010, ApJ, 720, 480

—. 2011, ApJ, 734, 98

Roberge, A., Welsh, B. Y., Kamp, I., Weinberger, A. J., & Grady, C. A. 2014, ApJ, 796, L11

Rodriguez-Franco, A., Martin-Pintado, J., & Fuente, A. 1998, A&A, 329, 1097

Sault, R. J., Teuben, P. J., & Wright, M. C. H. 1995, in Astronomical Society of the Pacific Conference Series, Vol. 77, Astronomical Data Analysis Software and Systems IV, ed. R. A. Shaw, H. E. Payne, & J. J. E. Hayes, 433

The Astropy Collaboration, Robitaille, Thomas P., Tollerud, Erik J., et al. 2013, A&A, 558, A33. https://doi.org/10.1051/0004-6361/201322068

van der Walt, S., Colbert, S. C., & Varoquaux, G. 2011, Computing in Science Engineering, 13, 22

van 't Hoff, M. L. R., Tobin, J. J., Trapman, L., et al. 2018, ApJL, 864, L23

van Terwisga, S. E., van Dishoeck, E. F., Cazzoletti, P., et al. 2019, A&A, 623, A150

Visser, R., van Dishoeck, E. F., & Black, J. H. 2009, A&A, 503, 323

Walsh, C., Millar, T. J., Nomura, H., et al. 2014, A&A, 563, A33

Walsh, C., Loomis, R. A., Öberg, K. I., et al. 2016, ApJ, 823, L10

Yen, H.-W., Koch, P. M., Liu, H. B., et al. 2016, ApJ, 832, 204

Zuckerman, B., Kim, S. S., & Liu, T. 1995, ApJ, 446, L79

Zuckerman, B., & Song, I. 2012, ApJ, 758, 77